Multidimensional Unstructured-Grid Liquid Rocket Engine Nozzle Performance and Heat Transfer Analysis

Ten-See Wang[*]

NASA Marshall Space Flight Center,Huntsville,Alabama,35812

The objective of this study is to conduct a unified computational analysis for computing design parameters such as axial thrust, convective and radiative wall heat fluxes for regeneratively cooled liquid rocket engine nozzles, so as to develop a computational strategy for computing those parameters through parametric investigations. The computational methodology is based on a multidimensional, finite-volume, turbulent, chemically reacting, radiating, unstructured-grid, and pressure-based formulation, with grid refinement capabilities. Systematic parametric studies on effects of wall boundary conditions, combustion chemistry, radiation coupling, computational cell shape, and grid refinement were performed and assessed. Under the computational framework of this study, it is found that the computed axial thrust performance, flow features, and wall heat fluxes compared well with those of available data and calculations, using a strategy of structured-grid dominated mesh, finite-rate chemistry, and cooled wall boundary condition.

Nomenclature

C_1, C_2, C_3, C_μ = turbulence modeling constants, 1.15, 1.9, 0.25, and 0.09.

C_p = heat capacity

D = diffusivity

H = total enthalpy

---

[*] Staff Consultant, Applied Fluid Dynamics Analysis Group, TD64, Senior Member AIAA.

h	= static enthalpy
I	= radiative intensity
K	= thermal conductivity
k	= turbulent kinetic energy
P	= pressure
Q	= heat flux
R	= recovery factor
r	= location coordinate
T	= temperature
T^+	= law-of-the-wall temperature
t	= time, s
u, v, w	= mean velocities in three directions
u_τ	= wall friction velocity
x	= Cartesian coordinates
α	= species concentration
ε	= turbulent kinetic energy dissipation rate
θ	= energy dissipation contribution
κ	= absorption coefficient
μ	= viscosity
μ_t	= turbulent eddy viscosity ($=\rho C_\mu k^2/\varepsilon$)
Π	= turbulent kinetic energy production
ρ	= density
σ	= turbulence modeling constants

τ = shear stress

Ω = direction vector. Ω^- denotes the leaving radiative intensity direction

ω = chemical species production rate

Subscripts

b = black body

c = convective

cl = centerline

p = off-wall (wall-function) point

r = radiative

t = turbulent flow

w = wall

0 = reference

I.   Introduction

The two major factors in rocket engine design, performance and integrity (convective heat transfer), are often conducted separately. As a result, the final design based on performance may have to be altered due to convective heating considerations, and vice versa, resulting in delays and compromises. Recently, radiative heating has been generating concerns due to renewed interest in hydrocarbon engines. Those combined motivated this study to perform and demonstrate a unified analysis for the computation of those design parameters in a simultaneous fashion. Systematic parametric studies on effects of wall boundary conditions, combustion chemistry, radiation coupling, computational cell shape, and grid refinement were performed and assessed, in order to come up with a strategy for efficient and realistic computations.

3

An axisymmetric nozzle axial force analysis,[1] and a conjugate convective heat transfer analysis[2] for the Block I Space Shuttle Main Engine (SSME) thruster were reported in the 1990's, using a structured-grid, multi-zone computational fluid dynamics (CFD) solver FDNS. As the requirements for parallel computing efficiency and faster grid generation arise, an unstructured-grid CFD methodology UNIC was developed recently through several activities, namely the launch vehicle base-heating,[3] Laser propulsion,[4] and stage-separation.[5] This unstructured-grid CFD methodology is refined in this study to conduct a series of unified axial force, convective and radiative heat transfer analyses, simulating SSME hot-firing at sea level. Both axisymmetric and three-dimensional analyses were performed and a final computational strategy reported.

II. Computational Methodology

The time-varying transport equations of continuity, species continuity, momentum, global energy (total enthalpy), turbulent kinetic energy, and turbulent kinetic energy dissipation can be written as:

$$\frac{\partial \rho}{\partial t} + \frac{\partial}{\partial x_j}(\rho u_j) = 0$$

$$\frac{\partial \rho \alpha_i}{\partial t} + \frac{\partial}{\partial x_j}(\rho u_j \alpha_j) = \frac{\partial}{\partial x_j}\left[\left(\rho D + \frac{\mu_t}{\sigma_\alpha}\right)\frac{\partial \alpha_i}{\partial x_j}\right] + \omega_i$$

$$\frac{\partial \rho u_i}{\partial t} + \frac{\partial}{\partial x_j}(\rho u_j u_i) = -\frac{\partial p}{\partial x_i} + \frac{\partial \tau_{ij}}{\partial x_j}$$

$$\frac{\partial \rho H}{\partial t} + \frac{\partial}{\partial x_j}(\rho u_j H) = \frac{\partial p}{\partial t} + Q_r + \frac{\partial}{\partial x_j}\left(\left(\frac{K}{C_p} + \frac{\mu_t}{\sigma_H}\right)\nabla H\right)$$

$$+ \frac{\partial}{\partial x_j}\left(\left((\mu + \mu_t) - \left(\frac{K}{C_p} + \frac{\mu_t}{\sigma_H}\right)\right)\nabla(v^2/2)\right) + \theta$$

$$\frac{\partial \rho k}{\partial t} + \frac{\partial}{\partial x_j}\left(\rho u_j k\right) = \frac{\partial}{\partial x_j}\left[\left(\mu + \frac{\mu_t}{\sigma_k}\right)\frac{\partial k}{\partial x_j}\right] + \rho(\Pi - \varepsilon)$$

$$\frac{\partial \rho \varepsilon}{\partial t} + \frac{\partial}{\partial x_j}\left(\rho u_j \varepsilon\right) = \frac{\partial}{\partial x_j}\left[\left(\mu + \frac{\mu_t}{\sigma_\varepsilon}\right)\frac{\partial \varepsilon}{\partial x_j}\right] + \rho\frac{\varepsilon}{k}\left(C_1\Pi - C_2\varepsilon + C_3\Pi^2 / \varepsilon\right)$$

where the energy dissipation contribution θ can be expressed as:

$$\theta = \frac{\partial}{\partial x_i}\left[\left(\mu + \mu_t\right)\left(u_j\frac{\partial u_i}{\partial x_j} - (2/3)u_i\frac{\partial u_j}{\partial x_j}\right)\right]$$

and the shear stress τ_{ij} can be expressed as:

$$\tau_{ij} = \left(\mu + \mu_t\right)\left(\frac{\partial u_i}{\partial x_j} + \frac{\partial u_j}{\partial x_i} - \frac{2}{3}\frac{\partial u_k}{\partial x_k}\delta_{ij}\right)$$

A predictor and corrector solution algorithm was employed to provide coupling of the fluid governing equations. A second-order central-difference scheme was employed to discretize the diffusion fluxes and source terms of the governing equations. For the convective terms, a second-order upwind total variation diminishing difference scheme was used in this effort. To enhance the temporal accuracy, a second-order backward difference scheme was employed to discretize the temporal terms. A point-implicit (operator splitting) method was employed to solve the chemistry system.

An extended k-ε turbulence model[6] was used to describe the turbulence. A 7-species, 9-reaction detailed mechanism[7] was used to describe the finite-rate, hydrogen/oxygen (H_2/O_2) afterburning chemical kinetics. The seven species are H_2, O_2, H_2O, O, H, OH, and N_2.

A modified wall function approach was employed to provide wall boundary layer solutions that are less sensitive to the near-wall grid spacing. Consequently, the model has combined the advantages of both the integrated-to-the-wall approach and the conventional law-of-the-wall

approach by incorporating a complete velocity profile and a universal temperature profile[7]. This approach is especially useful in three-dimensional (3-D) applications.

The convective heat transfer follows the modified Newtonian law

$$Q_c = \left(\rho u_\tau / T^+\right)\left(h_w - h_p - R\left(u_p^2 / 2\right)\right)$$

The radiative heat transfer is analyzed by solving the radiative transfer equation

$$(\Omega \cdot \nabla)I(r,\Omega) = -\kappa I(r,\Omega) + \kappa I_b(r)$$

Discrete ordinate method was used to solve the radiative transfer equation and H_2O is the major radiating medium. The spectral-line based weighted-sum-of-gray-gases model[8] was used to calculate the total emissivity and absorptivity of the radiating medium. Details of the numerical algorithm can be found in Ref's 3-5. The radiative heat flux is given by the integration of the wall leaving radiative intensities

$$Q_r = \int\limits_{n.\Omega^- < 0} I(r,\Omega^-)\left| n\Omega^- \right| d\Omega^-$$

III. Computational Grid Generation

The flowfields of four axisymmetric and four 3-D grids were computed during the course of this study. The results from two representative axisymmetric and two 3-D grids are reported for conciseness. These grids are hybrid grids and can be classified into two groups: the structure-grid dominated and the unstructured-grid dominated. Figure 1 shows the layout of an axisymmetric, unstructured-grid dominated hybrid grid ax1. It has four layers of structured (quadrilateral) grid surrounding the solid walls, while the rest of the domain filled with unstructured (triangular) cells. These structured-grid layers are used to ensure proper wall

6

boundary layer development. The layout of an axisymmetric, structure-cell dominated hybrid grid ax6 is shown in Fig. 2. The interior of the thruster and plume region is filled with quadrilateral cells, while the rest of the domain is filled with triangular cells. The structured-grid layers used in grid ax1 are also embedded in grid ax6, and in 3-D grids 3d6 and 3d9 (Figs 3-4), such that the boundary layer development for all grids is similar. Figure 3 shows the layout of the hybrid 3-D grid 3d6. It was constructed by rotating grid ax6 72 times for 360 degrees. Figure 4 shows the layout of the hybrid grid 3d9. These computational grids were generated using the software package GRIDGEN.[9] Table 1 shows the total number of points and cells in these four grids. The structured cells in grids 3d6 and 3d9 are hexahedral elements. The unstructured cells in grid 3d9 are tetrahedral elements, while the unstructured cells in grid 3d6 are prismatic elements. Note that all four grids were computed as a single zone, thus avoiding the interface complexities commonly seen in multi-zonal grids.

Table 1. Number of points and cells of the axisymmetric and 3-D grids.

grid	# points	# cells	# structured cells	# unstructured cells
ax1	17,509	30,578	2,016	28,562
ax6	17,391	17,710	15,300	2,410
3d6	1,286,934	1,275,120	1,101,600	173,520
3d9	418,165	1,732,081	227,984	1,504,097

IV. Boundary Conditions and Run Matrix

Fixed total condition was used for the inlet of the thruster and the outer boundary. A total pressure of 1 atm was specified for the outer boundary in order to simulate the nozzle hot-firing at sea level. No-slip boundary condition was specified for the thruster walls. Symmetry condition was applied to the centerline for axisymmetric cases. The CEC program[10] was used to obtain the chamber equilibrium species composition for use at the thruster inlet.

The run matrix is shown in Table 2. These cases were built up systematically in order to understand the grid effects such as cell shape and grid refinement, and the modeling effects such as chemistry, wall boundary condition, and radiation. For the convenience of presentation, abbreviated letters are used to represent different cases in the run matrix. For example, case fz represents parametric conditions of frozen chemistry and adiabatic wall, while case frcgr uses parametric conditions of finite-rate chemistry, cooled wall, with grid refinement and radiation coupling. Due to the limitation of current resources, grid refinement was not performed for the 3-D cases.

Table 2. Run matrix

case	chemistry	wall	grid refinement	radiation
fz	frozen	adiabatic	off	off
eq	equilibrium	adiabatic	off	off
fr	finite-rate	adiabatic	off	off
frc	finite-rate	cooled	off	off
frcr	finite-rate	cooled	off	on
frcg	finite-rate	cooled	on	off
frcgr	finite-rate	cooled	on	on

V.   Results and Discussion

The computations were performed on a cluster machine using four processors for each axisymmetric case and thirty-two processors for each 3-D case. A global time step of 1 μs was used. Figure 5 shows a comparison of the computed adiabatic wall temperatures for grid ax6. Similar, if not identical wall temperature profiles were obtained for grid ax1 and are not shown. The computed wall temperature for the frozen chemistry case is constant, indicating the conservation laws are satisfied. Those for the equilibrium and finite-rate chemistry cases increase first after the throat, due to the recombination of chemical species to become H_2O. The

8

temperatures for those two cases then decrease as H_2O dissociates. Of interest is the temperature for the equilibrium case, it drops continuously until it closes to that of the frozen flow, near the nozzle exit. This is expected since the stagnation temperature is very close to the chamber temperature with which the frozen composition was determined with an equilibrium solution. This also implies the equilibrium chemistry probably dissociates the H_2O at too fast a rate inside the nozzle. A specified cooled wall temperature profile[1] is also shown in Fig. 5 which was determined through a separate conjugate heat transfer calculation; this temperature profile is used later as a boundary condition to consider the effect of heat loss to the regenerative coolant channels.

Figure 6 shows the computed Mach number contours for cases fz and frcgr for grids ax1 and ax6, respectively; those for other cases are similar to those of case frcgr and are not shown. These figures show the captured nozzle flow features (nozzle shock, lip shock, triple point, Mach disc, shock reflection, and shear layer/shock interaction). In general, all cases capture the flow features reasonably well, except the frozen flow case in which a curved Mach disk was obtained. It can also be seen that the nozzle shocks appear to be sharper in the contours of the structured-cell dominated grid ax6 than those of the unstructured-element dominated grid ax1. The sharpest nozzle flow features are captured with grid refinement on grid ax6, while the added radiation changes the flow features only slightly.

The significance of a curved disk is that a large flow recirculation appears behind the curved disk. The occurrence of the curved disk may be attributed to the difference in thermodynamics between the frozen flow and chemically reacting flows. As shown in the centerline H_2O mass fraction, specific heat ratio and Mach number profiles in Fig. 7, the inability of recombining the species of the frozen flow results in much higher specific heat ratios than those of the reacting

flows, which in turn produces high Mach numbers along the centerline. The higher shock strength leads to higher total pressure loss across the shock, which causes the shock center to retreat and consequently an overall curved disk. On the other hand, the curves of equilibrium chemistry closely follow those of finite-rate chemistry. This is because the centerline temperatures drop continuously and are much lower than the chamber temperature (Fig. 8), hence the dissociation process occurring on the adiabatic wall is frozen on the centerline. Furthermore, the curved disk phenomenon happens both in grid ax1 and ax6, hence it is cell-shape independent and thermodynamically induced.

Figure 8 shows a comparison of the thruster centerline temperatures for grid ax6. The frozen chemistry gives the lowest bound while all other cases group together as an upper bound, while the result from Ref. 1 falls in between. As discussed above, the low frozen chemistry curve is caused by the thermodynamics. As for the result from Ref. 1, it is speculated that an older thermodynamics database was used then. A comparison of the thruster wall pressures is shown in Fig. 9. The computed results from all cases appear to group together and agree reasonably well with the test data. Figure 10 shows a comparison of thruster centerline pressures. All predictions agree reasonably well, except for the frozen flow case that deviates lower near the nozzle lip.

Figure 11 shows the computed convective heat fluxes for grid ax6. As expected, the peak convective heat fluxes occur at the throat (x = 0) for all cases. The refined grid gives a slightly lower peak heat flux. Radiation does not affect the convective heat flux, because the maximum radiative heat flux is about two orders-of-magnitude lower than that of convection (Fig. 12). All predictions compare reasonably well with those of the three other methods.[2,11] Result from Fig. 11 demonstrates that both the momentum and thermal wall boundary layers were captured

reasonably well with the current methodology. The difference in the initial heat fluxes is caused by the difference in ways of initiating the boundary layers among different methods and the significance of which is negligible in comparison to the peak heat flux.

Figure 12 shows the computed radiative heat flux for grid ax6 while cooled wall, finite-rate chemistry, and grid refinement were used as operating conditions. As expected, high radiative heating occurs inside the combustion chamber within which the high temperature and high H_2O concentration are prevalent. As the propulsive flow expands past the throat, the temperature drops, hence the low radiative heat flux. The peak radiative heat flux is about two orders of magnitude lower than that of the convective heat flux, which is reasonable for a hydrogen fueled engine. In current methodology, the injector faceplate is modeled as a black body. In order to compare the predicted radiation with that of a plume radiation code GASRAD,[12] which does not model the injector faceplate, another run was performed by setting the temperature of the injector faceplate to 300 deg. K, effectively turning off the black body radiation. The structured-grid solution from Ref. 1 was used as input for GASRAD radiation calculation, since GASRAD can not read unstructured-grid information. It can be seen that the result from turning off the blackbody radiation at the inlet, using a weighted-sum-of-gray-gases (WSGG) absorption model, compares reasonably well with that of GASRAD in which a narrow band (NB) absorption model was used. It should be pointed out that GASRAD reads in flow solution for a decoupled radiation solution, and current methodology solves the flow equations and radiative transfer equation simultaneously. The computed peak value is higher when the black body radiation is included at the inlet, as expected. It is also noted that GASRAD was developed for the prediction of plume radiation, hence it does not consider the re-radiation from the solid walls. In addition, it solves the line-of-sight equation and not the radiative transport equation.

11

Table 4. Comparison of SSME thrust chamber specific impulses (ISP's) for axisymmetric cases

	ax1	ax6
fz	438.7	439.7
eq	455.6	456.0
fr	455.2	455.6
frc	452.4	452.6
frcg	452.9	453.7
frcgr	452.5	453.3
Data	453.3	

Table 4 shows the comparison of computed SSME thrust chamber specific impulses, or the axial thrust performances for the axisymmetric cases. The frozen flow calculations give too low an axial force, even with the adiabatic wall assumption that assumes zero wall heat loss. This is again caused by inadequate heat capacity distributions forced by a fixed species composition. The reacting flow (with adiabatic wall) cases overpredict the data for about 2~3 s, with the equilibrium case giving the highest values. When the wall heat loss is considered (case frc), the axial force predictions become very close to the data. The quadrilateral cell dominated grid ax6 appears to predict slightly better ISP's than those of the triangular cell dominated grid ax1. Within grid ax6, the grid refinement and radiation options (case frcgr) provide the best agreement.

Figure 13 shows the computed temperature contours for grid 3d6, case frc. Similar to the Mach number contours, the temperature contours also show the captured nozzle flow physics such as the nozzle shock, lip shock, triple point, Mach disc, shock reflection, and shear layer/shock interaction. Two perpendicular planes are used to give the Mach disc a three-dimensional feel. The high temperature in the mixing layer indicates afterburning.

Figure 14 shows a comparison of computed thruster centerline temperatures. The centerline temperature of grid 3d6 matches that of grid ax6 reasonable well, except inside the chamber where the temperature of grid 3d6 is slightly lower. Figure 15 compares the wall pressures. The

wall pressures of grid 3d6 and ax6 overlap and both compare reasonably well with the data. Figure 16 compares the centerline pressures. The centerline pressure of grid 3d6 coincides with that of grid ax6, until the nozzle lip where the pressure of grid ax6 is slightly higher.

Figure 17 shows a comparison of convective wall heat fluxes. The computed 3-D heat fluxes agree reasonably well with those of other methods, while the predictions of grid 3d6 overlap with those of grid ax6. The radiation does not affect the convective heat fluxes of grid 3d6, again due to the relative low radiative heat fluxes inside a H_2/O_2 engine. Figure 18 shows a comparison of the computed radiative wall heat fluxes. Similar to the result of the axisymmetric cases (Fig. 12), the computed 3-D radiative fluxes using a weighted-sum-of-gray gases absorption model compares reasonably well with that of GASRAD using a narrow band absorption model, when the blackbody radiation at the inlet is turned off; And the predicted radiative heat flux is higher while the blackbody radiation at the inlet is turned on.

Table 5. Comparison of SSME thrust chamber specific impulses (ISP's) for 3-D cases

	3d6	3d9
fz	439.6	436.5
eq	456.4	453.3
fr	454.9	452.5
frc	453.2	450.0
frcr	453.1	449.9
Data	453.3	

Table 5 shows the comparison of computed specific impulses for the 3-D cases. The qualitative trend among the cases is very similar to the corresponding axisymmetric cases (Table 4). The results of grid 3d9 are consistently lower than those of grid 3d6. This is because the effective cell density of grid 3d9 is less than that of 3d6, although the total number of cells in grid 3d9 is higher than that of grid 3d6 (Table 1). As a general rule of thumb, the accuracy of two tetrahedral cells is approximately equivalent to that of one hexagonal cell. On the other

13

hand, since the number of cells in grid 3d9 is more than those in grid 3d6, it costs more to run grid 3d9. This demonstrates that the structured-cell dominated grid 3d6 is more favorable both in terms of accuracy and computational efficiency, similar to the findings in the axisymmetric cases. This also agrees with the result of Huynh's Fourier analysis[13] that the upwind scheme prefers structured meshes. Within grid 3d6, again the result of case frc compares very well with that of the measurement, while the addition of radiation (case frcr) changes the value only slightly.

VI. Conclusions

Unified computational analyses for computing the design parameters such as the axial thrust, convective and radiative wall heat fluxes for hydrogen-fueled liquid rocket engine thrusters were conducted, in order to develop a computational strategy for computing those design parameters through parametric investigations. The computational methodology is based on a multi-dimensional, finite-volume, turbulent, chemically reacting, radiating, unstructured-grid, and pressure-based formulation. Systematic parametric studies on effects of wall boundary conditions, combustion chemistry, radiation coupling, computational cell shape, and grid refinement were performed and assessed. Under the computational framework of this study, it is found that the structured-mesh performed more favorably than the unstructured-mesh. The effect of radiation coupling was shown to not make an appreciable difference, while that of grid refinement sharpens shock capturing. Finite-rate chemistry option performed better than that of the equilibrium chemistry, while the frozen chemistry option is undesirable, due to thermodynamics considerations. For regeneratively cooled engines, incorporating the effect of heat loss drastically improves the axial force predictions. The computed flow physics, axial

thrust performance, and wall heat fluxes compared well with those of available test data and design calculations, when the desired computational strategy (structured-grid dominated mesh, finite-rate chemistry, and cooled wall) was used.

Acknowledgments

References

[1]Wang, T.-S. and Chen Y.-S., "Unified Navier-Stokes Flowfield and Performance Analysis of Liquid Rocket Engines," *Journal of Propulsion and Power*, Vol. 9, No. 5, 1993, pp.678-685.

[2]Wang, T.-S., and Luong, V., "Hot-Gas-Side and Coolant-Side Heat Transfer in Liquid Rocket Engine Combustors," *Journal of Thermophysics and Heat Transfer*, Vol. 8, No. 3, 1994, pp.524-530.

[3]Chen, Y.-S., Liu, J., Zhang, S., and Mallapragada, P., "An Integrated Tool for Launch Vehicle Base-Heating Analysis," Final Report, Engineering Sciences, Inc., Huntsville, AL, December, 2001.

[4]Wang, T.-S., Chen, Y.-S., Liu, J., Myrabo, L.N., and Mead, F.B. Jr., "Advanced Performance Modeling of Experimental Laser Lightcraft," *Journal of Propulsion and Power,* Vol. 18, No. 6, 2002, pp. 1129-1138.

[5]Chen. Y.-S., Zhang S., and Liu, J., "Stage Separation Performance Analysis Project," Final Report, Engineering Sciences, Inc., Huntsville, AL, June, 2002.

[6]Chen, Y.-S., and Kim, S. W., "Computation of Turbulent Flows Using an Extended k-ε Turbulence Closure Model," NASA CR-179204, Oct. 1987.

[7]Wang, T.-S., Droege, A., D'Agostino, M., Lee, Y.-C., and Williams, R., "Asymmetric Base-Bleed Effect on X-33 Aerospike Plume Induced Base-Heating Environment," *Journal of Propulsion and Power,* Vol. 20, No. 3, 2004, pp. 385-393.

[8]Liu, J., Shang, H.-M., Chen, Y.-S., and Wang, T.-S., "GRASP: A General Radiation Simulation Program," AIAA Paper 97-2559, June, 1997.

[9]Steinbrenner, J.P., Chawner, J.R., and Fouts, C., "Multiple Block Grid Generation in the interactive Environment," AIAA Paper 90-1602, June 1990.

[10]Svehla, R.A., and McBride, B.J., "FORTRAN IV Computer Program for Calculation of Thermodynamic and Transport Properties of Complex Chemical Systems," NASA TN D-7056, Jan. 1973.

[11]Naraghi, M.H.N., Dunn, S., and Coats, D., "A Model for Design and Analysis of Regeneratively Cooled Rocket Engines," AIAA Paper 2004-3852, July, 2004.

[12]Reardon, J., and Lee, Y.-C., "A Computer Program for Thermal Radiation from Gaseous Rocket Plumes (GASRAD)," Report RTR 014-9, REMTech, Inc., Huntsville, AL, Dec. 1979.

[13]Huynh, H.T., "Analysis and Improvement of Upwind and Centered Schemes on Quadrilateral and Triangular Meshes," AIAA Paper 2003-3541, June 2003.
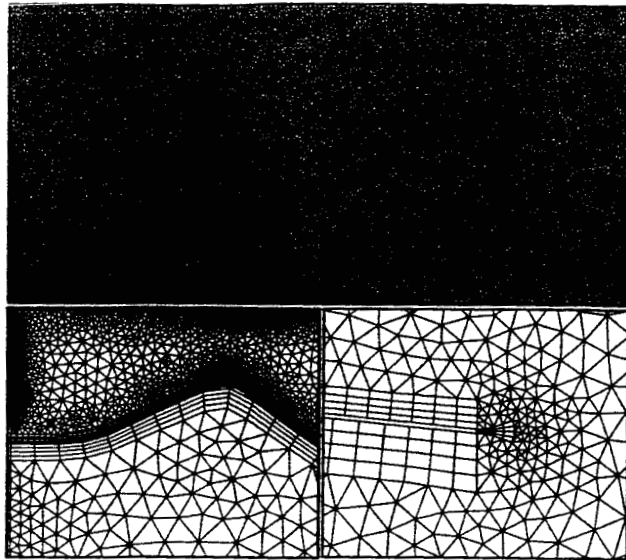
Fig. 1 The layout of hybrid grid ax1. Top: the overall grid. Bottom left: close-up near the throat. Bottom right: close-up near the nozzle lip.
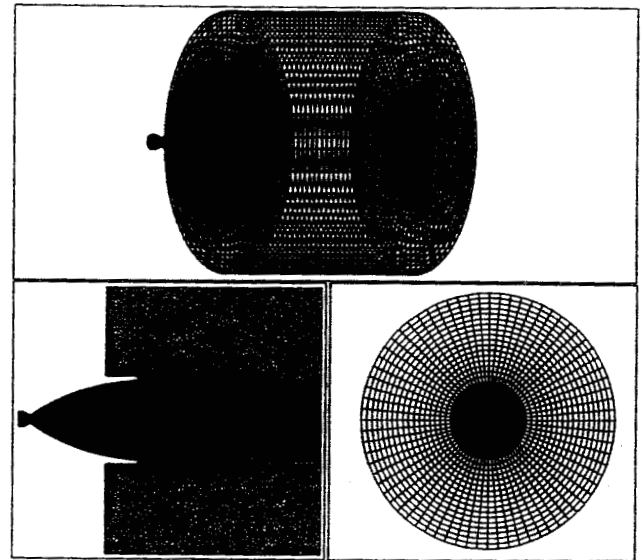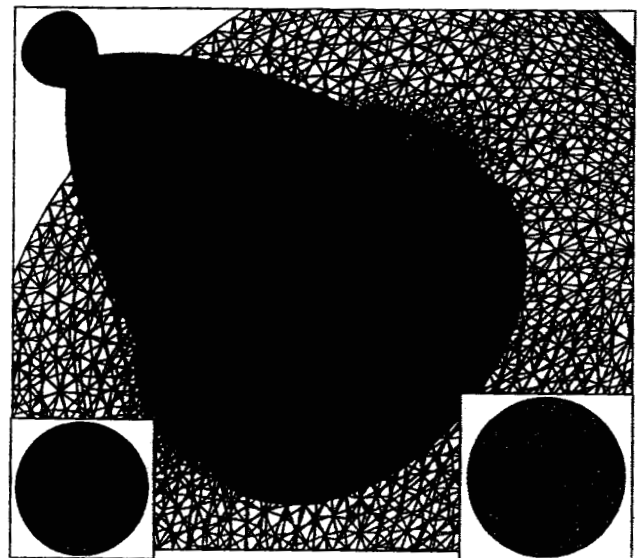

Fig. 3 Layout of hybrid grid 3d6. Upper figure: an overall view. Lower left: a cross-sectional cut through the axis. Lower right: the exit plane.
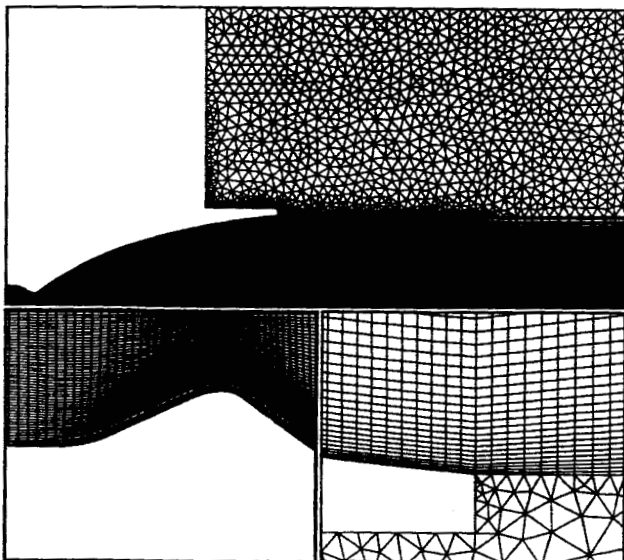
Fig. 2 The layout of hybrid grid ax6. Top: the overall grid. Bottom left: close-up near the throat. Bottom right: close-up near the nozzle lip.

Fig. 4 Layout of hybrid grid 3d9. Lower left insert: the cross-sectional cut of the thruster inlet. Lower right insert: the cross-sectional cut of the exit plane.
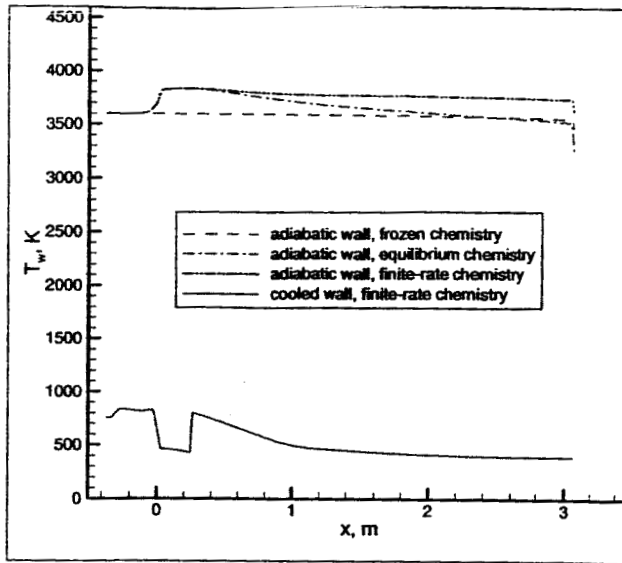
Fig. 5   A comparison of computed and specified regeneratively cooled wall temperatures for grid ax6.
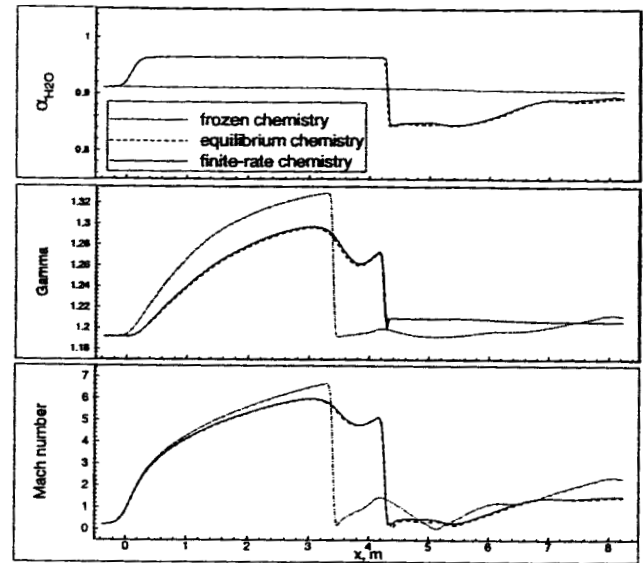
Fig. 7 A comparison of computed centerline H_2O mass fractions, specific heat ratios and Mach numbers for grid ax6.
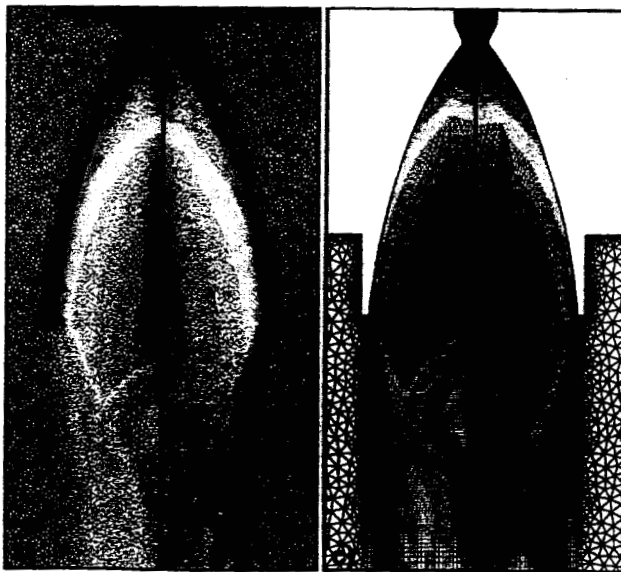
Fig. 6   Computed Mach number contours. a) case fz, grid ax1; b) case frcgr, grid ax1; c) case fz, grid ax6; and d) case frcgr, grid ax6.
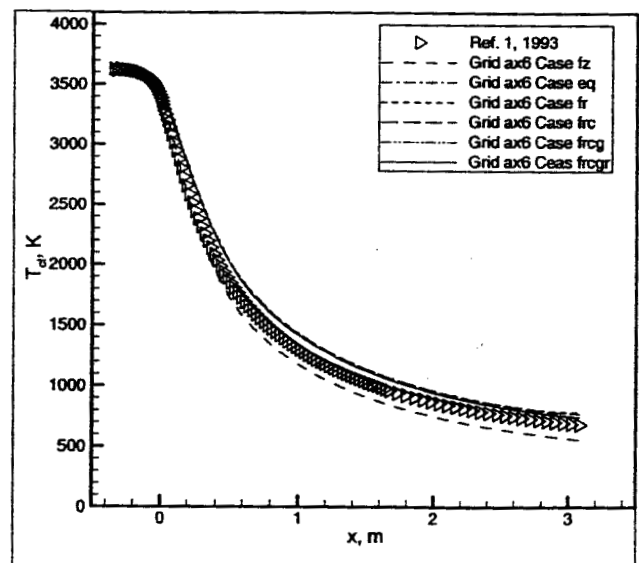
Fig. 8   A comparison of thruster centerline temperatures for grid ax6.
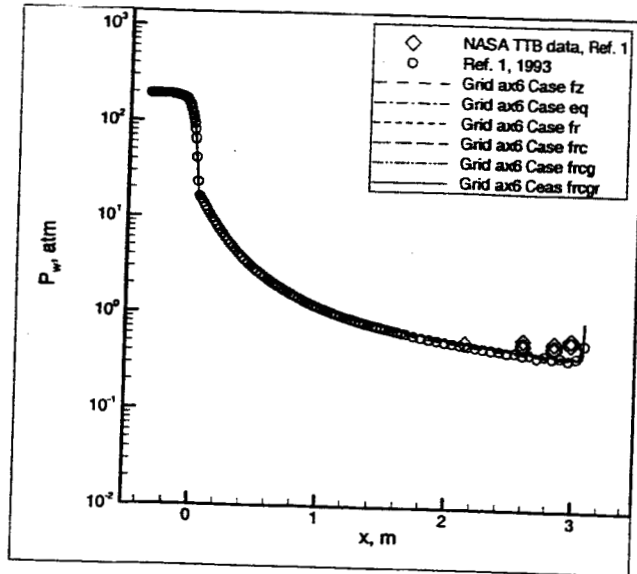
Fig. 9 A comparison of thruster wall pressures for grid ax6.
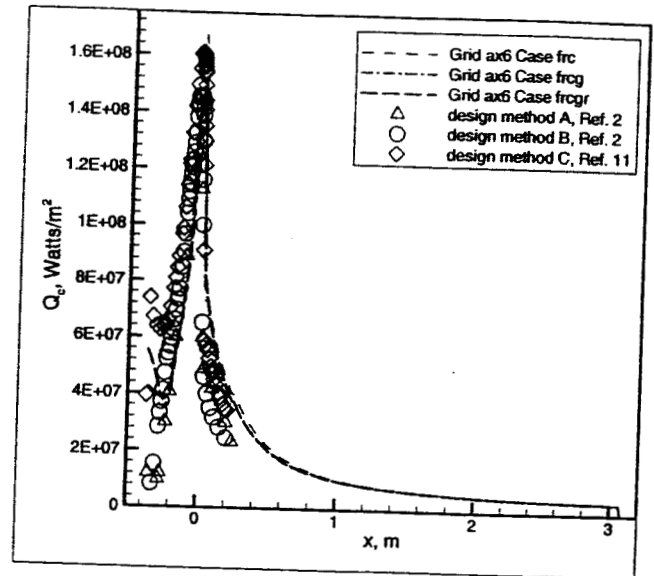
Fig. 11 A comparison of convective wall heat fluxes for grid ax6.
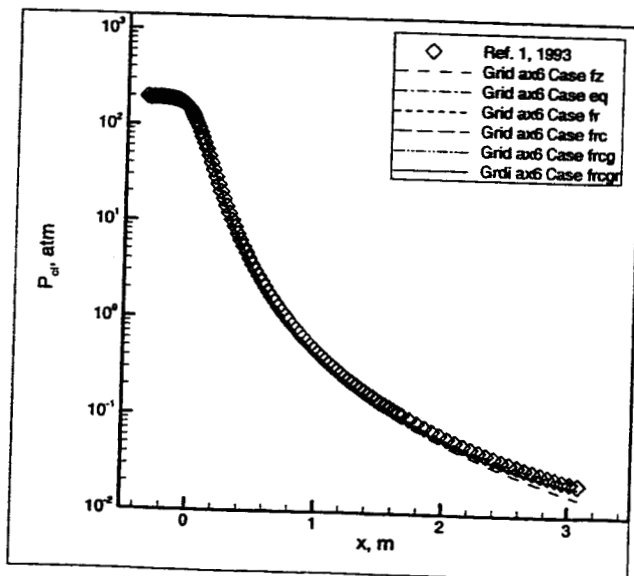
Fig. 10 A comparison of thruster centerline pressures for grid ax6.
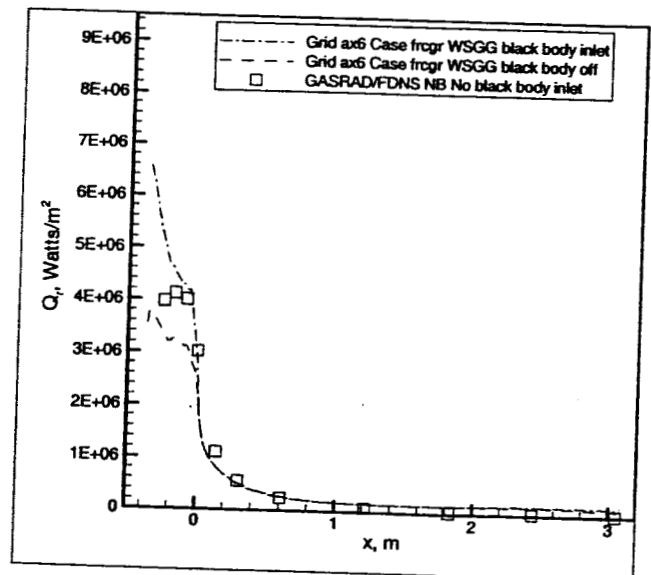
Fig. 12 A comparison of radiative wall heat fluxes for grid ax6.
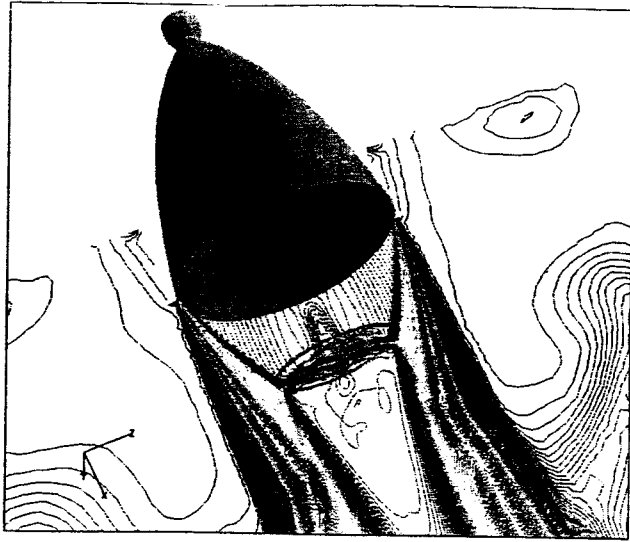
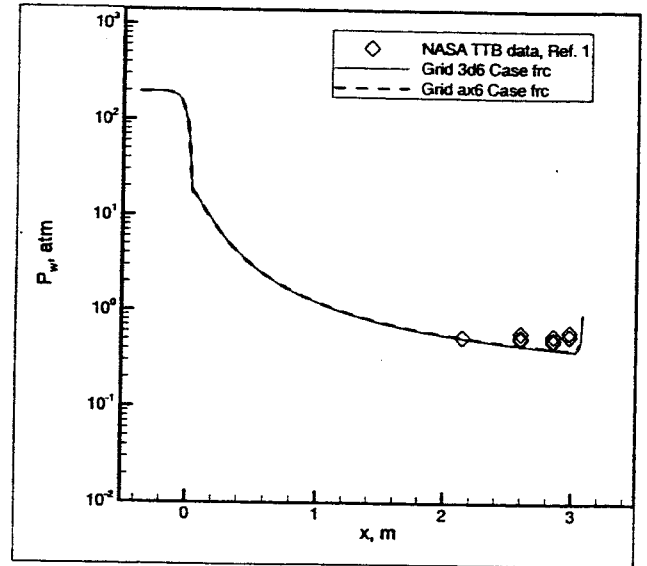**Fig. 13 Computed temperature contours for grid 3d6, case frc.**

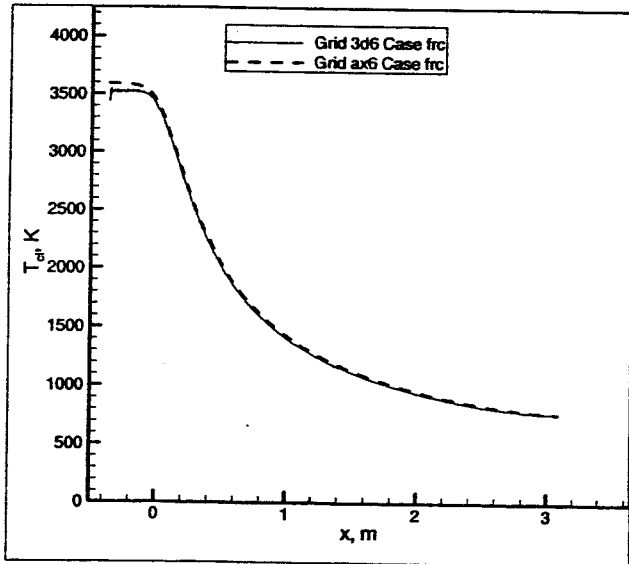**Fig. 15 A comparison of thruster wall pressures.**

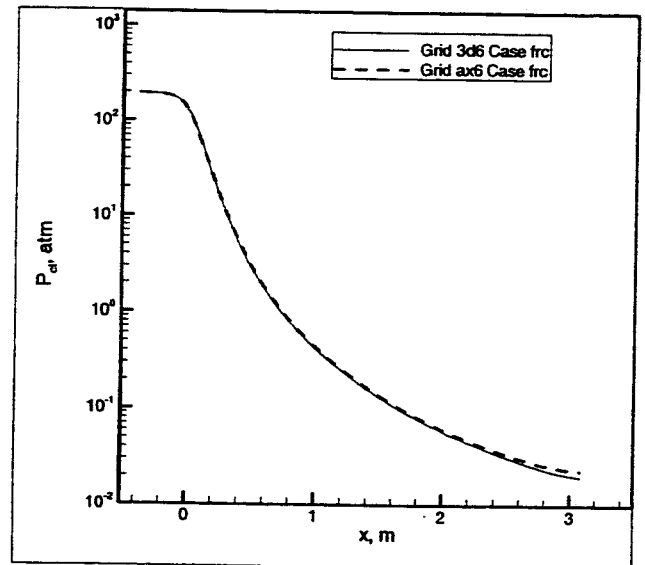**Fig. 14 A comparison of thruster centerline temperatures.**

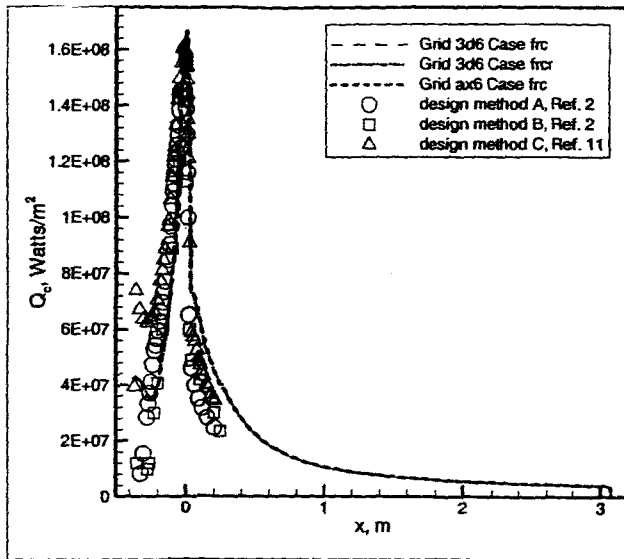**Fig. 16 A comparison of thruster centerline pressures.**
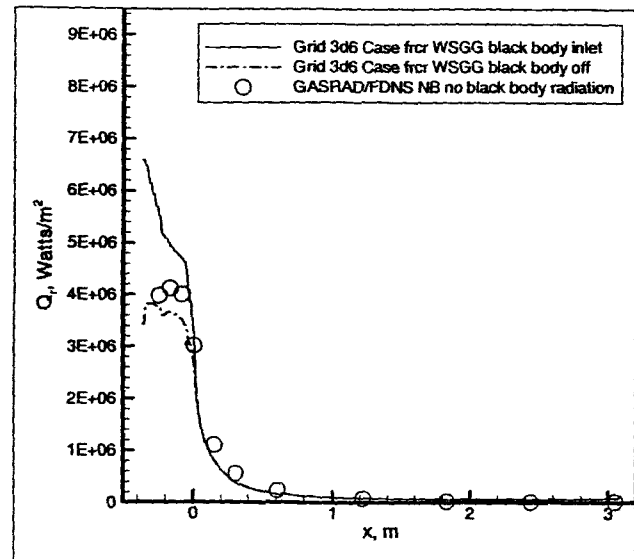
20

Fig. 17 A comparison of convective wall heat fluxes.

Fig. 18 A comparison of radiative wall heat fluxes.